ZHAO, X., WU, F., HU, H., LI, J., SUN, Y., WANG, J., ZOU, G., CHEN, X., WANG, Y., FERNANDEZ, C. and PENG, Q. 2024. N-decorated main-group $MgAl_2O_4$ spinel: unlocking exceptional oxygen reduction activity for Zn-air batteries. *Small* [online], 20(28), article number 2311268. Available from: https://doi.org/10.1002/smll.202311268

N-decorated main-group $MgAl_2O_4$ spinel: unlocking exceptional oxygen reduction activity for Zn-air batteries.

ZHAO, X., WU, F., HU, H., LI, J., SUN, Y., WANG, J., ZOU, G., CHEN, X., WANG, Y., FERNANDEZ, C. and PENG, Q.

2024

This is the peer reviewed version of the following article: ZHAO, X., WU, F., HU, H., LI, J., SUN, Y., WANG, J., ZOU, G., CHEN, X., WANG, Y., FERNANDEZ, C. and PENG, Q. 2024. N-decorated main-group $MgAl_2O_4$ spinel: unlocking exceptional oxygen reduction activity for Zn-air batteries. Small, 20(28), article number 2311268, which has been published in final form at https://doi.org/10.1002/smll.202311268. This article may be used for non-commercial purposes in accordance with Wiley Terms and Conditions for Use of Self-Archived Versions. This article may not be enhanced, enriched or otherwise transformed into a derivative work, without express permission from Wiley or by statutory rights under applicable legislation. Copyright notices must not be removed, obscured or modified. The article must be linked to Wiley's version of record on Wiley Online Library and any embedding, framing or otherwise making available the article or pages thereof by third parties from platforms, services and websites other than Wiley Online Library must be prohibited.
Supplementary materials are appended after the main text of this document.

OpenAIR @RGU

This document was downloaded from https://openair.rgu.ac.uk

SEE TERMS OF USE IN BOX ABOVE

DISTRIBUTED UNDER LICENCE

N-Decorated Main-Group $MgAl_2O_4$ Spinel: Unlocking Exceptional Oxygen Reduction Activity for Zn-Air Batteries

*Xue Zhao, Fengqi Wu, Haidong Hu, Jinyu Li, Yong Sun, Jing Wang, Guodong Zou,**
*Xiaobo Chen, Yong Wang, Carlos Fernandez, and Qiuming Peng**

X. Zhao, F. Wu, H. Hu, J. Li, Y. Sun, J. Wang, G. Zou, Q. Peng
State Key Laboratory of Metastable Materials Science and Technology Yanshan University, Qinhuangdao 066004, P.R. China
E-mail: zouguodong@ysu.edu.cn; pengqiuming@ysu.edu.cn
X. Chen
School of Engineering RMIT University, Carlton, VIC 3053, Australia
Y. Wang
College of Chinese Medicine, Beijing University of Chinese Medicine Beijing 100029, P.R. China
C. Fernandez
School of Pharmacy and life sciences Robert Gordon University Aberdeen AB107GJ, UK

Abstract

The development of economical and efficient oxygen reduction reaction (ORR) catalysts is crucial to accelerate the widespread application rhythm of aqueous rechargeable zinc-air batteries (ZABs). Here, a strategy is reported that the modification of the binding energy for reaction intermediates by the axial N-group converts the inactive spinel $MgAl_2O_4$ into the active motif of $MgAl_2O_4$-N. It is found that the introduction of N species can effectively optimize the electronic configuration of $MgAl_2O_4$, thereby significantly reducing the adsorption strength of *OH and boosting the reaction process. This main-group $MgAl_2O_4$-N catalyst exhibits a high ORR activity in a broad pH range from acidic and alkaline environments. The aqueous ZABs assembled with $MgAl_2O_4$-N shows a peak power density of 158.5 mW cm^{-2}, the long-term cyclability over 2000 h and the high stability in the temperature range from -10 to 50 °C, outperforming the commercial Pt/C in terms of activity and stability. This work not only serves as a significant candidate for the robust ORR electrocatalysts of aqueous ZABs, but also paves a new route for the effective reutilization of waste Mg alloys.

Keywords

main-group catalyst, ORR, recycle, spinel, ZABs

1. Introduction

Aqueous zinc-air batteries (ZABs) are attractive energy stor- age systems due to their low cost, high safety and high energy density.[1] The theoretical capacity density of ZABs (1086 W h kg^{-1}) can reach 2–5 times of Li-ion batteries, yet the consumption is only ≈ \$10 kW^{-1} per hour.[2] However, the unique semi-open structure of aqueous ZABs makes them vulnerable to environmental temperature, which severely restricts their practical applications, such as polar inspections, deep sea exploration, and mining.[3] Especially, the reduced ionic conductivity of the aqueous electrolyte at low temperatures increases the resistance of the battery, and consequent degrades its performance.[4] Notably, a large number of disposable ZABs have been maturely used in portable hearing aids, but the high cost and dissatisfied stability of precious metal-based catalysts (such as Pt and Ru) have hindered the commercial development of rechargeable ZABs.[5] As a result, the development of catalysts with high performance, low cost, and good structural stability operated in extreme environments for oxygen reduction reaction (ORR) has been a great challenge.

Basically, the precious platinum group metals are plagued by low crustal abundances, and high costs.[6] Recently, nitrogen-coordinated dispersed transition metal centers (M-N-C) have gained attention due to their intrinsically high activity, comparable to that of Pt/C catalyst, offering an alternation for Pt ORR catalysts.[7] However, the reported transition metal centers in ORR experiments have predominantly focused on Fe, Co, Ni, Mn and Cu, with their coordination primarily relying on nitrogen atoms.[8] These incompletely coordinated transition metals exhibit limited durability during ORR. While the research on M-N-Cs have focused on transition metals, recent studies have demonstrated that main-group metals (for example, Mg, Sn, Sb, Bi), which were typically considered to be catalytically inert due to the closed d-band shells, can be activated via engineering the atomic M-N_x moieties, resulting in promising catalytic reactivity.[9] Especially for the ORR process, main-group M-N-Cs have exhibited rivaling activity compared to the state-of-the-art Fe-based counterparts, while alleviating the transition metal-induced Fenton reactions.[10] However, they are still constrained by the poor structural stability inherent in single-atom catalysts.[11]

The spinel compounds of AB_2X_4 (A, B = metal, X = chalcogen) have arisen great interests because of their wide applications in magnetism, electronics and catalysis, as well as energy storage and conversion.[12] For instance, $MgAl_2O_4$, as one of the most common spinel structures found in nature, boasts remarkable chemical and thermal stability.[13] Recent studies have demonstrated that structural modifications of spinels, such as the introduction of defects or doping (transition metals or non-metal elements), can significantly enhance their intrinsic catalytic activity.[14] But the catalytic activity of transition metal doping catalysts is highly dependent on external factors such as the elemental composition, the coordination number, and the oxidation states of cations.[14a,b,15] The variability of oxidation states often results in the reduction of catalyst stability.[16] In addition to transition metals doping, the introduction of non-metal atoms has been demonstrated as a highly effective approach to modify the surface properties and electronic structure of materials.[14c,d] This strategy not only enriches the chemical characteristics of materials but also exhibits remarkable potential in enhancing the intrinsic activity of electrocatalysts. This insight provides inspiration for the development of $MgAl_2O_4$ with high catalytic performance.

In present work, we employed a straightforward ball- milling solid-solution assistant pyrolysis approach to synthesize $MgAl_2O_4$ spinel catalysts with nitrogen atoms adsorption, denoted as $MgAl_2O_4$-N. This catalyst not only exhibits remarkably high ORR activity in alkaline environments, but also demonstrates superiority over Pt/C in neutral and mildly acidic conditions. Most significantly, it displays outstanding long-term cycling stability exceeding 2000 hours in rechargeable aqueous ZABs and excellent stability in a wide temperature range. Both microstructure observations and density functional theory (DFT) calculations confirm that the successful nitrogen adsorption on the $MgAl_2O_4$-N is the underlying mechanism, which delivers its exceptional cathodic performance in ZABs.

2. Results and Discussion

2.1. Catalyst Characteristics

The homogenous and porous $MgAl_2O_4$-N sample has been synthesized via a ball-milling solid-solution assistant pyrolysis approach, as illustrated in Figure S1, Supporting Information. Specifically, the alloy composed of Mg and $Mg_{17}Al_{12}$ is formed by mixing Mg and Al powders by high-energy ball milling pre-treatment. Moreover, X-ray diffraction (XRD) pat- terns show the product is completely transformed to $Mg_{17}Al_{12}$ when the Al content increases to 40 wt% (Figure S2a, Supporting Information). Simultaneously, high resolution transmission electron microscopy (HRTEM) image (Figure S2b, Supporting Information) confirms that the $Mg_{17}Al_{12}$ phase is uniformly dispersed in Mg matrix with an average particle size of ≈5 nm (Figure S2c, Supporting Information). This strategy relative to a solid-solution precursor provides some distinctive advantage to control the structure and size of the resultant spinel product.[17]

To probe the reaction process, the variation of phase composition has been investigated. XRD patterns (Figure S2d, Supporting Information) reveal that the Mg matrix has been oxidized to MgO and N-doping graphene (NC) after pyrolysis treatment in a mixed atmosphere, while $Mg_{17}Al_{12}$ phase has been transformed to $MgAl_2O_4$ at elevated temperature. Subsequently, the by-product MgO is removed by 1 M HCl. A large number of N atoms in the environment are adsorbed on the surface of $MgAl_2O_4$, resulting in the formation of $MgAl_2O_4$-N (Figure S3, Supporting Information). The main chemical process can be summarized as follows:

$$Mg + Mg_{17}Al_{12} + CO + NH_3 \rightarrow MgO + MgAl_2O_4 - N\ (\text{graphene}) + H_2O \qquad (1)$$

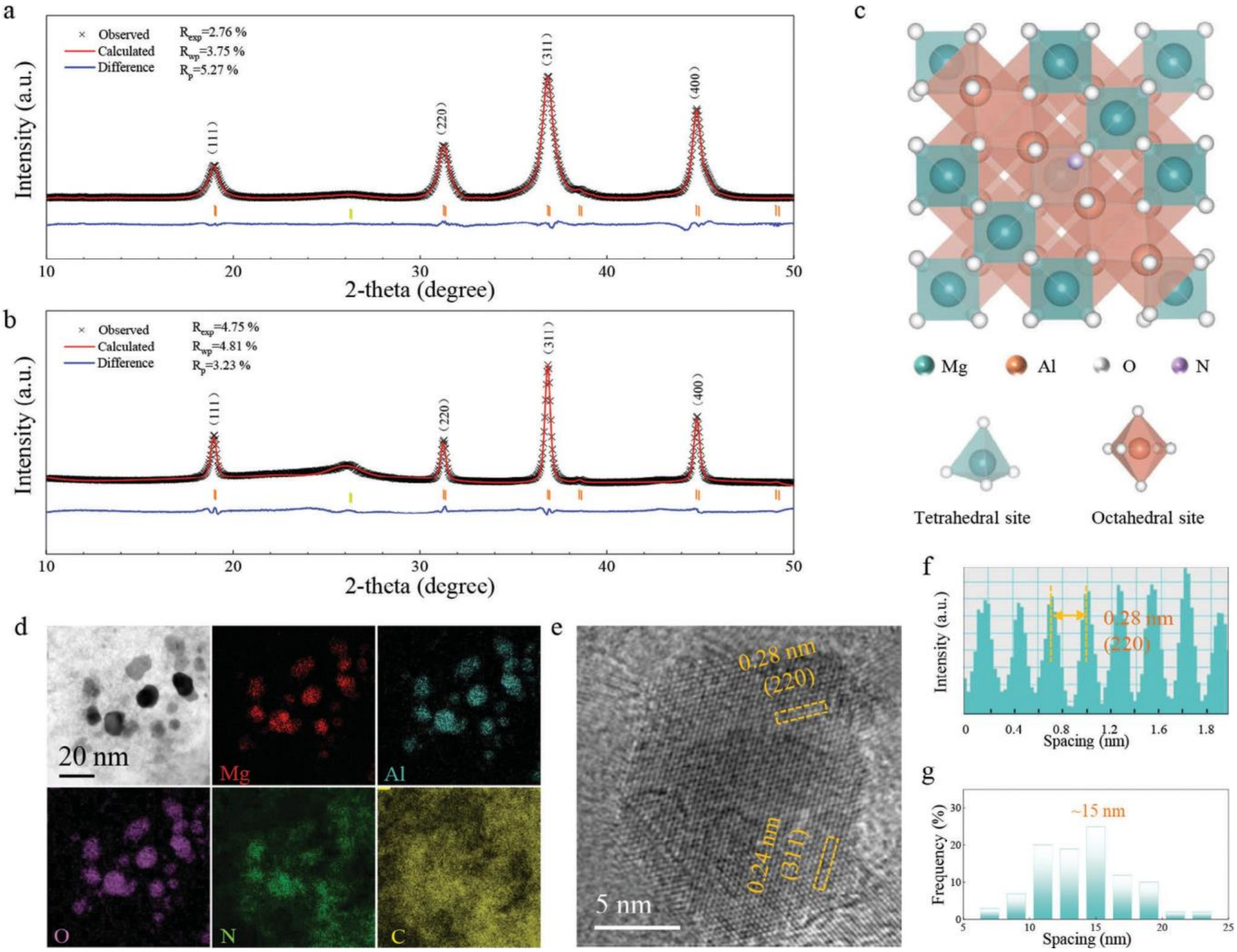

Figure 1. Phase and microstructure. Refined XRD patterns of the $MgAl_2O_4$-N a) and the $MgAl_2O_4$ b), respectively. c) Crystal structure of the $MgAl_2O_4$-N. d) EDX elemental mapping of the as-prepared $MgAl_2O_4$-N. e) HRTEM image of the as-prepared $MgAl_2O_4$-N. f) The line profiles for atomic imaging intensity analysis. g) Size distribution of the $MgAl_2O_4$-N particles.

XRD and inductively coupled plasma-mass spectrometry results (Table S1, Supporting Information) show that the $MgAl_2O_4$-N concentration increases with the increment of Al content. However, the Mg:Al atomic ratio remains 1:2, suggesting its structure stability. The phase structure of these catalysts was analyzed by X-ray diffraction (XRD) with the typical pattern presented in **Figure 1**a,b. The Rietveld refinement analysis on phase structure (Figure 1a,b) indicates that $MgAl_2O_4$-N possesses a structure with a lattice parameters of 8.4713 A and a space group of *Fd-3m*. Comparatively, the $MgAl_2O_4$ possesses a structure with a lattice parameters of 8.4350 A and a space group of *Fd-3m*. It demonstrates that $MgAl_2O_4$-N retains the original spinel structure, except for the little change of lattice constant after N adsorption (Figure 1c). The possible impurity phases, such as MgO and Al_3O_4, have hardly been detected. Scanning electron microscope images (Figure S4, Supporting Information) reveal that both of $MgAl_2O_4$-N and NC show a three-dimensional honeycomb-like morphology with many gradient macropores in a combination of micropores, relative to the self-template MgO removal. As shown with the Brunauer-Emmett-Teller (Figure S4, Supporting Information), the N_2 isotherms for $MgAl_2O_4$-N at 77 K were type-I isotherms corresponding to microspores and then changed to type-IV isotherms with hysteresis, which indicates mesopores from oxide aggregation. During the pyrolysis treatment, the Mg matrix is supposed to be converted into MgO or/and $MgAl_2O_4$; Subsequently, only the by-product MgO is removed after acid washing, leaving a small number of pores. That leads to the fact that the specific surface area of $MgAl_2O_4$-N (258.5 $m^2 g^{-1}$) is slightly smaller than NC (279.1 $m^2 g^{-1}$). A typical low magnification transmission electron microscopy (TEM) image (Figure 1d) reveals that the nanoparticles on the NC substrate were composed of the $MgAl_2O_4$-N particles. In addition, the energy-dispersive spectra (EDS) elemental mapping images confirm the N atoms are successfully adsorbed on the oxide surface of the $MgAl_2O_4$-N (Figure 1d). HRTEM images (Figure 1e–g) reveal that the $MgAl_2O_4$-N phase possesses an average particle size of ≈15 nm, which was smaller than that of the $MgAl_2O_4$ (Figure S5, Supporting Information). Additionally, the average lattice parameter of the $MgAl_2O_4$-N is ≈ 0.28 nm, corresponding to the (220) lattice planes of face center cubic spinel, which was consistent with $MgAl_2O_4$. This indicates that the nitrogen atoms are not incorporated into the $MgAl_2O_4$ lattice, but adsorbed on the surface of the $MgAl_2O_4$ particles.

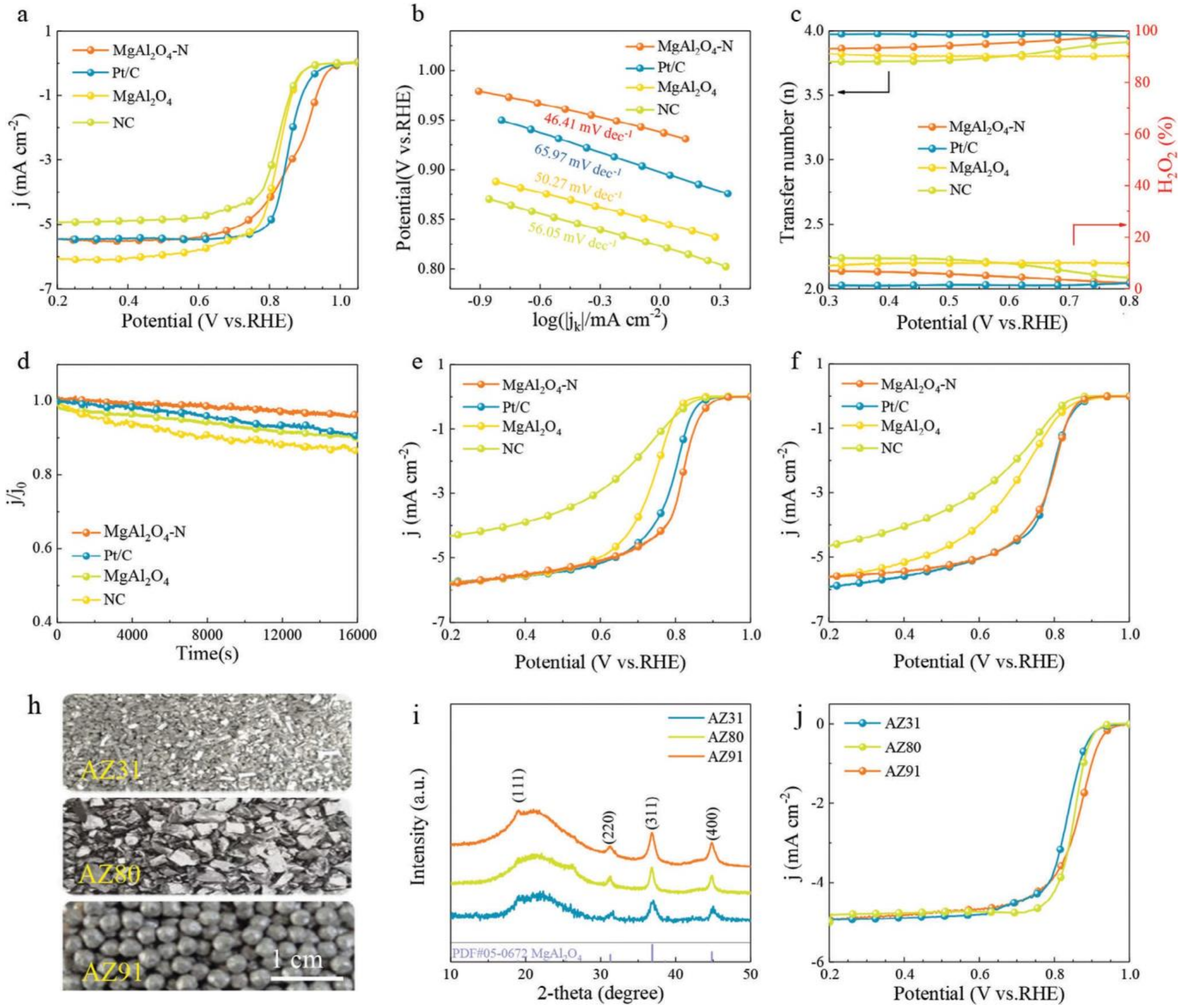

Figure 2. Electrochemical properties. a) Steady-state polarization curves in a O_2-saturated 0.1 M KOH solution at 1600 rpm and 10 mV s^{-1}. b) Tafel plots obtained from Figure 2a. c) The H_2O_2 yield and the electrons transfer rate. d) CA test of the catalysts at 0.6 V with 1,600 rpm in a O_2-saturated 0.1 M KOH solution. e) Steady-state polarization curves in O_2-saturated pH = 7 electrolyte at 1600 rpm and 10 mV s^{-1}. f) Steady-state polarization curves in a O_2-saturated pH = 5 electrolyte at 1600 rpm and 10 mV s^{-1}. Macroscopic morphology h), XRD i) and electrochemical performances j) of waster Mg alloys.

X-ray photoelectron spectroscopy (XPS) measurements were further performed to clarify surface electronic properties of the $MgAl_2O_4$-N (Figure S6 and Table S2, S3, Supporting Information). The presence of the N-O peak in the O 2p and N 2p spectra, coupled with the absence of Mg-N in the Mg 2p and Al-N in the Al 2p peaks, suggests that nitrogen atoms are adsorbed at the O site rather than doped into the lattice (Figure S6b,c, Supporting Information).[18] Compared to the $MgAl_2O_4$, the Mg 2p peak slightly shifts to the lower band energy, due to the influence of N atoms on the surface (Figure S6d, Supporting Information). Meanwhile, the oxidation peak of Al 2p in the $MgAl_2O_4$-N catalyst shifts to higher binding energy, indicating the higher valence state (Figure S6e, Supporting Information).[19] Therefore, as evidenced by TEM, EDS elemental mapping, and XPS test, it is confirmed that the N atoms is adsorbed on the O sites of the $MgAl_2O_4$-N particles.

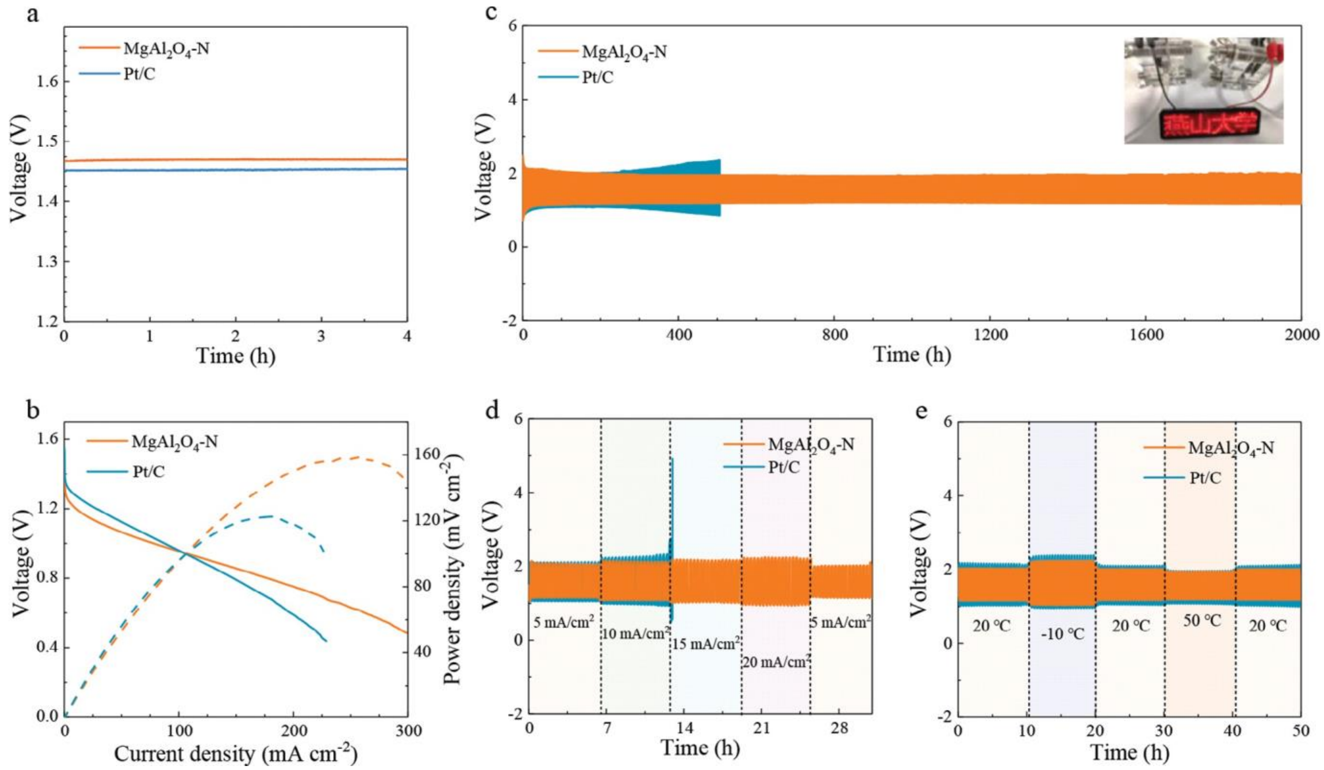

Figure 3. ZABs performances. a) Open circuit voltage curves. b) Discharge polarization curves and corresponding areal power density curves. c) Long- term cyclic stability tests at a current density of 10 mA cm^{-2}. d) The galvanostatic charge-discharge curves at room temperature with various current densities. e) The galvanostatic charge-discharge curves of 10 mA cm^{-2} at different temperatures.

2.2. Catalytic Properties

The ORR electrocatalytic performance of MgAl$_2$O$_4$-N has been evaluated in a O$_2$-saturated 0.1 M KOH solution with a rotating ring disk electrode. All the potentials are calibrated to the reversible hydrogen electrode (versus RHE). As examined by linear sweep voltammetry (LSV) curves at 1600 rpm in a 0.1 M O$_2$- saturated KOH electrolyte, the MgAl$_2$O$_4$-N exhibits an encouraging onset potential (E_{onset} = 0.964 V) and an excellent half-wave potential ($E_{1/2}$ = 0.881 V) (**Figure 2**a), which are more active than the MgAl$_2$O$_4$ ($E_{1/2}$ = 0.821 V), and the NC ($E_{1/2}$ = 0.820 V). Meanwhile, the $E_{1/2}$ of the MgAl$_2$O$_4$-N is even 30 mV higher than that of commercial 20 wt% Pt/C (0.851 V). The Tafel plots are calculated on the basis of the LSV data to evaluate the kinetics for ORR electrocatalysis, and a smaller Tafel slope means a faster electrocatalytic reaction.[20] As demonstrated in Figure 2b, a Tafel slope of 46.41 mV dec^{-1} is achieved on the MgAl$_2$O$_4$- N electrocatalyst, which is lower than that of the Pt/C electrocatalyst (65.97 mV dec^{-1}). This discrepancy underscores the accelerated ORR kinetics on the MgAl$_2$O$_4$-N electrocatalyst. The MgAl$_2$O$_4$-N electrocatalyst also exhibits a stable electron transfer number of 3.9 within the ORR potential range, corresponding to a low H_2O_2 selectivity of 5% (Figure 2c; Figure S7, Supporting Information).

In addition, long-term durability of the catalyst has been assessed by accelerated stability tests between 0.6 and 1.0 V at 100 mV s^{-1} in a 0.1 M KOH. The MgAl$_2$O$_4$-N shows a negligible decay of $E_{1/2}$ after 20 000 cyclic voltammetry cycles (Figure S8, Supporting Information), which underlines its high stability. To deeply gain insight into the high durability of the MgAl$_2$O$_4$-N structure, we carried out XPS measurements to monitor changes in the catalysis configuration before and after accelerated durability tests (Figure S9 and Table S4, Supporting Information). The structures remain intact except for the carbon atoms absorbing additional oxygen. A small decay (2.3%) of J_L (limited current density) is obtained, which may be attributed to the reduction of ECSA (electrochemical active surface area) after cycling (Figure S10a–c, Supporting Information). Moreover, 95.7% normalized current is retained at 0.7 V after a chronoamperometry (CA) durability test of 16 000 s for the MgAl$_2$O$_4$-N (Figure 2d), while only 90.1% normalized current is retained for Pt/C, signifying the stability of the MgAl$_2$O$_4$-N catalyst. Furthermore, the methanol tolerance of the MgAl$_2$O$_4$-N is assessed by injecting methanol solution during the CA test. The current density of the MgAl$_2$O$_4$-N (Figure S10d, Supporting Information) shows excellent tolerance to methanol crossover in contrast to that of commercial Pt/C.

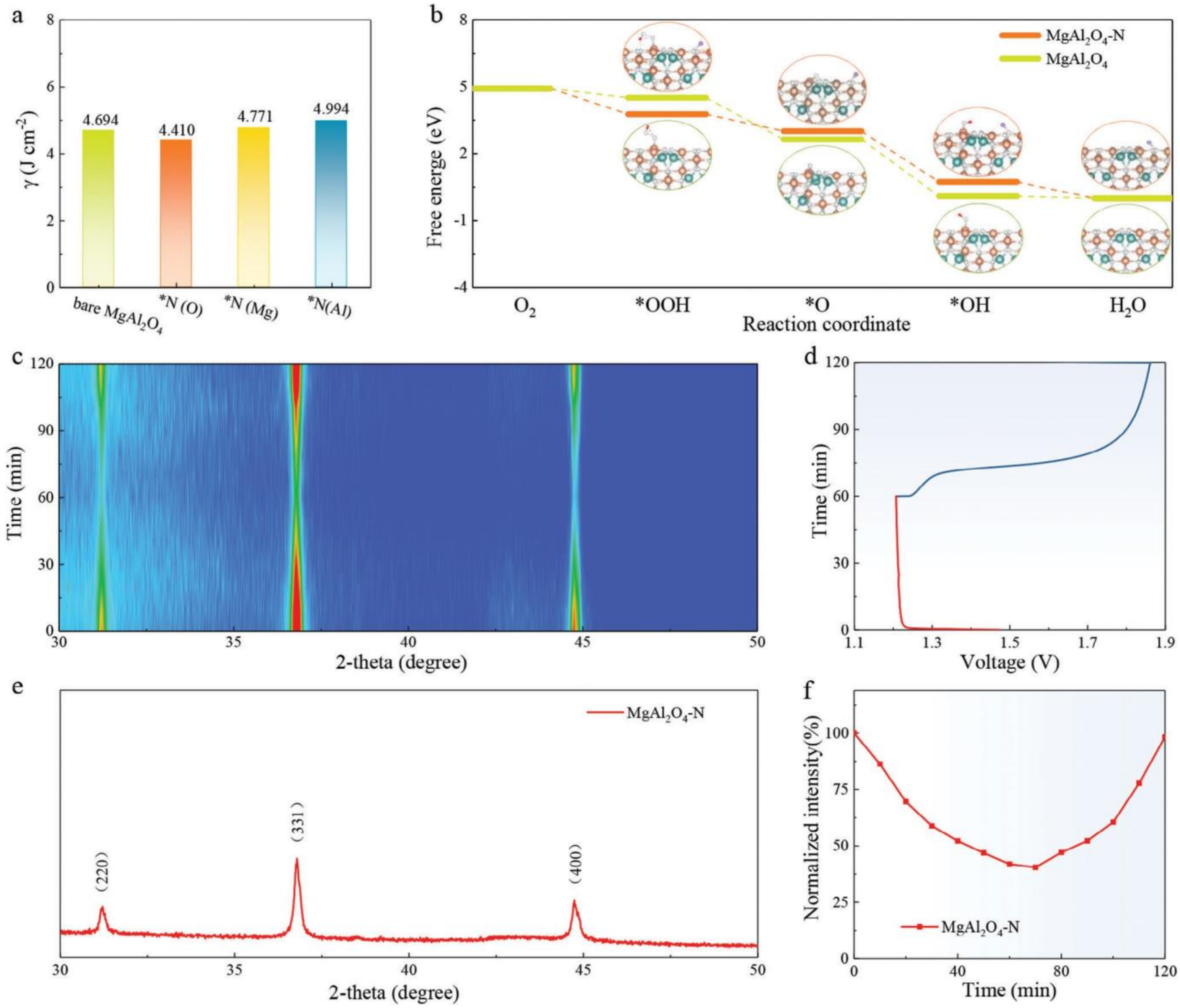

Figure 4. Catalytic mechanisms. a) The adsorption energy of oxygen at different sites. b) Theoretical ORR overpotential calculated from the Gibbs free energy diagram. c) in situ XRD intensity map of ZABs with the $MgAl_2O_4$-N electrode during discharging and charging d). e) XRD patterns at 60 min during discharge. f) Intensity changes of the $MgAl_2O_4$-N peak at 36.70° during ZABs operation.

To explore the wide applications of the MgAl2O4-N in different environments, we tested its ORR activity in both neutral and weakly acidic conditions. Note that the MgAl2O4-N achieves the highest ORR activity with E_{onset} of 0.886 V and $E_{1/2}$ of 0.812 V in the neutral conditions (Figure 2e; Figure S11, Supporting Information), and E_{onset} of 0.859 V and $E_{1/2}$ of 0.786 V in the acidic conditions (Figure 2f; Figure S12, Supporting Information), out-performing those of Pt/C and other control samples. Tafel curves are also plotted based on the polarization curves to assess the kinetic process of catalysts. In the potential region of ORR catalysis, the MgAl2O4-N manifest the smallest Tafel slopes of 46.41 and 49.46 mV dec−1 in neutral and acidic conditions, respectively. Furthermore, the lowest current density loss is attained in the $MgAl_2O_4$-N after CA testing, demonstrating that the $MgAl_2O_4$-N possesses outstanding activity and stability in a wide pH range from weakly acidic to highly alkaline conditions.

Waste Mg alloys, such as AZ31(Mg-3Al-1Zn), AZ80(Mg-8Al- 0.3Zn) and AZ91(Mg-9Al-1Zn) alloys were utilized as raw materials to minimize financial cost (Figure 2h). XRD results revealed that Mg matrix is able to convert into N-doped carbon under a mixed atmosphere of CO and NH_3. The eutectic $Mg_{17}Al_{12}$ phase can be transformed to the $MgAl_2O_4$-N spinel catalysts (Figure 2i and Figure S13, Supporting Information). Compared with the AZ31 (a very low $MgAl_2O_4$-N concentration, $E_{1/2}$ = 0.841 V), both of AZ80 ($E_{1/2}$ = 0.857 V) and AZ91 ($E_{1/2}$ = 0.860 V) samples exhibit better ORR performances in aqueous alkaline environments, respectively (Figure 2j).

2.3. ZABs Performances

The ZABs with the $MgAl_2O_4$-N electrocatalyst loaded on the cathode side are assembled to evaluate its potential applications. A high open-circuit voltage of 1.47 V is achieved, which is slightly higher than that of Pt/C (1.45 V), in consistent with the higher ORR activity (Figure 3a). The ZABs with the MgAl2O4-N electrocatalyst also exhibit higher polarization, compared to the counterparts with the Pt/C (Figure 3b), which displays a peak power density of 158.5 mW cm^{-2}, dramatically outperforming the commercial Pt/C (122 mW cm^{-2}).

A 2000 h long-term test has been performed at a current density of 5 mA cm^{-2} (Figure 3c) for the $MgAl_2O_4$-N cathode, overwhelming the counterparts equipped with the Pt/C benchmark and other reported catalysts (Table S5, Supporting Information). The rate performance of batteries at various current densities by galvanostatic discharge-charge tests (Figure 3d) shows the $MgAl_2O_4$-N displays a step-like voltage response with the discharge current density varying from 5 to 20 mA cm^{-2}. Furthermore, the charge-discharge voltage gap could be efficiently restored to ~0.86 V when the current density returned to 5 mA cm^{-2}, indicating its excellent high-rate performance and robust durability. More attractively, this high performance can also be achieved in the temperature range from −10 to 50 °C, illus- trating its wide-temperature industrial applications (Figure 3e).

2.4. Catalytic Mechanism

To elucidate the adsorption site of N atoms on the $MgAl_2O_4$ spinel surface, DFT calculations have been performed (Figure 4a and Figure S14, Supporting Information). The formation enthalpy of N atoms adsorbing on the O of AlO_6 in $MgAl_2O_4$ is lower than other adsorption modes, even lower than the pristine $MgAl_2O_4$. Hence, it is believed that N atoms are adsorbed at O sites in the resultant product $MgAl_2O_4$-N, which is consistent with the experimental results. The free energy map at 0 V (Figure 4b and Figure S14, Supporting Information) shows that the strong binding of *OH in the last step (*OH→H2O) is an uphill process in the $MgAl_2O_4$ model, which is the potential rate-determining step. However, the $MgAl_2O_4$-N model optimizes the adsorption strength of *OH, resulting in a significant reduction in the overpotential. In fact, the -N can be regarded as an electron-withdrawing group, which attracts electrons from the Al atoms. As a consequent, Al exhibits a more positive charge state,[21] weakening the bonding between Al and *OH intermediates.[22] Conversely, this effect on the binding energy of *OH intermediates on Mg atoms can be neglected owing to far space distance from –N group. Therefore, the octahedral center Al serves as an active site, which endows the $MgAl_2O_4$-N with superior electrochemical ORR activity.

This high ORR activity has further been clarified by in situ XRD measure on ZABs assembled in a tailor-made mold (Figure 4c,d and Figure S15, Supporting Information). Initially, both the $MgAl_2O_4$-N and the $MgAl_2O_4$ exhibit three prominent peaks of spinel (220), (331), and (400) at 31.2°, 36.8°, and 44.7°, respectively (Figure 4e). For the $MgAl_2O_4$-N sample, these peaks gradually become weak during the discharging process, suggesting continuous adsorption of oxygen molecules on the cathode surface during the ORR process (Figure 4f).[23] In contrast, there is no noticeable change of spinel peaks in the $MgAl_2O_4$ sample, demonstrating that the $MgAl_2O_4$ is inactive (Figure S15, Supporting Information). Meanwhile, it is found that the spinel signals in the ZABs with the $MgAl_2O_4$-N air cathode are recovered after the charging process, which indicates that the active sites are completely reversible (Figure 4f). In general, the deposition of ZnO would gradually clog active sites and hamper oxygen gas diffusion, degrading the discharge performance.[24] However, the ZnO signal of the $MgAl_2O_4$-N has hardly been captured during the whole steady discharge plateaus process, confirming the effectively suppressed metal oxidization on the cathode.

3. Conclusion

A main-group spinal $MgAl_2O_4$-N catalyst with high oxygen reduction reaction activity has firstly been achieved through a strategy of varying the binding energies for reaction intermediates by the axial N-group. The microstructure of $MgAl_2O_4$-N catalyst has been well confirmed through TEM, EDS elemental mapping, and XPS tests. This main-group $MgAl_2O_4$-N catalyst shows out-standing electrocatalytic activity ($E_{1/2}$ = 0.881) and cycling stability (over 20 000 cycles) across a wide pH range, outperforming both pristine $MgAl_2O_4$ and commercial Pt/C catalysts. The ZABs loaded with the $MgAl_2O_4$-N catalyst exhibit exceptional durability (over 2000 hour) under challenging conditions, including varying charge-discharge rates and an extensive temperature range from −10 °C to 50 °C. Both experimental and calculated results con- firm that the activity of MgAl2O4-N is closely associated with the adsorption of N atoms on the surface oxygen atoms of MgAl2O4, wherein the electron transformation from Al to N weakens the bonding between Al and *OH intermediates, enhancing its ORR activity. This highly active and stable main-group spinel in ZABs cathodes presents a promising and cost-effective alternative to Pt-based catalysts.

Acknowledgements

The author greatly acknowledge the financial support by National Natural Science Foundation (52171126, 52331033, and 52202374), "S&T Program of Hebei" (236Z1020G), the Hebei Natural Science Foundation (C2022203003, E2023203255, and E2022203167), Science Research Project of Hebei Education Department (BJK2024087) and Ministry of Education Yangtze River Scholar Professor Program of China (T2020124).

Conflict of Interest

The authors declare no conflict of interest.

References

[1] a) T. Wei, Q. Li, G. Yang, C. Wang, *Adv. Energy Mater.* **2019**, *9*, 1901480; J. Fu, Z. P. Cano, M. G. Park, A. Yu, M. Fowler, Z. Chen, *Adv. Mater. 2017, 29,* 1604685; c) Q. Liu, Z. Pan, E. Wang, L. An, G. Sun, *En- ergy Storage Mater.* **2020**, *27*, 478; d) R. Kumar, S. Prabhakaran, S. Ramakrishnan, S. Karthikeyan, A. Kim, D. Kim, D. Yoo, *Small* **2023**, *19*, 2207096.

[2] a) H.-F. Wang, Q. Xu, *Matter* **2019**, *1*, 565; b) J. Du, Z. Gu, L. Yan, Y. Yong, X. Yi, X. Zhang, J. Liu, R. Wu, C. Ge, C. Chen, *Adv. Mater.* **2017**, *29*, 1701268.

[3] S. Liu, R. Zhang, J. Mao, Y. Zhao, Q. Cai, Z. Guo, *Sci. Adv.* **2022**, *8*, eabn5097.

[4] a) T. Cui, Y. P. Wang, T. Ye, J. Wu, Z. Chen, J. Li, Y. Lei, D. Wang, Y. Li, *Angew. Chem., Int. Ed.* **2022**, *61*, 202115219; b) Y. Zhang, H. Qin, M. Alfred, H. Ke, Y. Cai, Q. Wang, F. Huang, B. Liu, P. Lv, Q. Wei, *Energy Storage Mater. 2021, 42, 88.*

[5] a) Z. P. Cano, D. Banham, S. Ye, A. Hintennach, J. Lu, M. Fowler, Z. Chen, Nat. Energy 2018, 3, 279; b) H. F. Wang, C. Tang, Q. Zhang, Adv. Funct. Mater. 2018, 28, 1803329.

[6] a) U. Martinez, S. Komini Babu, E. F. Holby, H. T. Chung, X. Yin, P. Zelenay, *Adv. Mater.* **2019**, *31*, 1806545; b) X. Xie, C. He, B. Li, Y. He, D. A. Cullen, E. C. Wegener, A. J. Kropf, U. Martinez, Y. Cheng, M. H. Engelhard, *Nat. Catal.* **2020**, *3*, 1044; c) M. Zhao, R. Yang, Y. Wei, J. Su, X. Wang, N. Zhang, P. Sun, D. Chen, Y. Zhao, *Nano Today* **2022**, *44*, 101493.

[7] a) N. Guo, H. Xue, R. Ren, J. Sun, T. Song, H. Dong, Z. Zhao, J. Zhang, Wang, L. Wu, *Angew. Chem., Int. Ed.* **2023**, *62*, 202312409; b) S. Liu, Z. Li, C. Wang, W. Tao, M. Huang, M. Zuo, Y. Yang, K. Yang, L. Zhang, S. Chen, Nat. Commun. 2020, 11, 938; c) J. Li, S. Chen, N. Yang, M. Deng, S. Ibraheem, J. Deng, J. Li, L. Li, Z. Wei, Angew. Chem., Int. Ed. 2019, 131, 7109.

[8] a) K. Liu, J. Fu, Y. Lin, T. Luo, G. Ni, H. Li, Z. Lin, M. Liu, *Nat. Commun.* **2022**, *13*, 2075; b) C.-X. Zhao, J.-N. Liu, J. Wang, C. Wang, X. Guo, X.-Y. Li, X. Chen, L. Song, B.-Q. Li, Q. Zhang, *Sci. Adv.* **2022**, *8*, eabn5091;

[9] J. Chen, H. Li, C. Fan, Q. Meng, Y. Tang, X. Qiu, G. Fu, T. Ma, *Adv. Mater.* **2020**, *32*, 2003134; d) J. Li, M. Chen, D. A. Cullen, S. Hwang, M. Wang, B. Li, K. Liu, S. Karakalos, M. Lucero, H. Zhang, *Nat. Catal.* **2018**, *1*, 935.

[9] a) Q. Wang, K. Liu, J. Fu, C. Cai, H. Li, Y. Long, S. Chen, B. Liu, Li, W. Li, *Angew. Chem., Int. Ed.* **2021**, *133*, 25445; b) F. Xu, C. Qu, Q. Lu, J. Meng, X. Zhang, X. Xu, Y. Qiu, B. Ding, J. Yang, F. Cao, *Sci. Adv.* **2022**, *8*, eabm7489; c) Z. Teng, Q. Zhang, H. Yang, K. Kato, W. Yang, Y.-R. Lu, S. Liu, C. Wang, A. Yamakata, C. Su, *Nat. Catal.* **2021**, *4*, 374; d) Y. Cao, S. Chen, S. Bo, W. Fan, J. Li, C. Jia, Z. Zhou, Q. Liu, L. Zheng, F. Zhang, *Angew. Chem., Int. Ed.* **2023**, *62*, 202303048.

[10] a) T. Wang, X. Cao, H. Qin, L. Shang, S. Zheng, F. Fang, L. Jiao, *Angew. Chem., Int. Ed.* **2021**, *60*, 21237; b) F. Luo, A. Roy, L. Silvioli, D. A. Cullen, A. Zitolo, M. T. Sougrati, I. C. Oguz, T. Mineva, D. Teschner, S. Wagner, *Nat. Mater.* **2020**, *19*, 1215.

[11] H. Hu, J. Wang, B. Cui, X. Zheng, J. Lin, Y. Deng, X. Han, *Angew. Chem., Int. Ed.* **2022**, *134*, 202114441.

[12] a) J. Hemberger, P. Lunkenheimer, R. Fichtl, H.-A. Krug von Nidda, V. Tsurkan, A. Loidl, *Nature* **2005**, *434*, 364; b) X. Xie, Y. Li, Z.-Q. Liu, M. Haruta, W. Shen, *Nature* **2009**, *458*, 746; c) Z. Wang, P. Wu, X. Zou, S. Wang, L. Du, T. Ouyang, Z. Liu, *Adv. Funct. Mater.* **2023**, *33*, 2214275.

[13] A. K. Schmidt-Verma, A. M. Renner, M. Wilhelm, C. Bohr, Y. Goenuellue, E. Rudigier-Voigt, S. Mathur, *Adv. Eng. Mater.* **2021**, *23*, 2000738.

[14] a) G. Tian, X. Liu, C. Zhang, X. Fan, H. Xiong, X. Chen, Z. Li, B. Yan, Zhang, N. Wang, *Nat. Commun.* **2022**, *13*, 5567; b) T. Wu, S. Sun, J. Song, S. Xi, Y. Du, B. Chen, W. A. Sasangka, H. Liao, C. L. Gan, G. G. Scherer, *Nat. Catal.* **2019**, *2*, 763; c) J. Sun, H. Xue, Y. Zhang, X.-L. Zhang, N. Guo, T. Song, H. Dong, Y. Kong, J. Zhang, Q. Wang, *Nano Lett.* **2022**, *22*, 3503; d) M. Chen, N. Kitiphatpiboon, C. Feng, Q. Zhao, A. Abudula, Y. Ma, K. Yan, G. Guan, *Appl. Catal. B-Environ.* **2023**, *330*, 122577.

[15] L. Wei, H. E. Karahan, S. Zhai, H. Liu, X. Chen, Z. Zhou, Y. Lei, Z. Liu, Chen, *Adv. Mater.* **2017**, *29*, 1701410.

[16] F. T. Haase, A. Rabe, F.-P. Schmidt, A. Herzog, H. S. Jeon, W. Frandsen, V. Narangoda, I. Spanos, K. Friedel Ortega, J. Timoshenko, *J. Am. Chem. Soc.* **2022**, *144*, 12007.

[17] C. Si, Y. Wang, J. Zhang, H. Gao, L. Lv, L. Han, Z. Zhang, *Nano Energy* **2016**, *23*, 105.

[18] L. Tao, Y. Yang, H. Wang, Y. Zheng, H. Hao, W. Song, J. Shi, M. Huang, D. Mitlin, *Energy Storage Mater.* **2020**, *27*, 212.

[19] H. Bai, L. Liang, P. Cao, H. Zhang, S. Chen, H. Yu, X. Quan, *Appl. Catal B-Environ.* **2024**, *343*, 123527.

[20] R. Ma, E. Song, Y. Zhou, Z. Zhou, G. Liu, Q. Liu, J. Liu, Y. Zhu, J. Wang, *Energy Storage Mater.* **2017**, *6*, 104.

[21] a) X. F. Li, S. Q. Cheng, Y. Q. Zhou, W. H. Ouyang, S. Li, B. X. Liu, J. B. Liu, *Small* **2022**, *18*, 2202623; b) M. Cho, J. T. Song, S. Back, Y. Jung, J. Oh, *ACS Catal.* **2018**, *8*, 1178.

[22] Y. Gu, B. J. Xi, H. Zhang, Y. C. Ma, S. L. Xiong, *Angew. Chem., Int. Ed.* **2022**, *134*, 202202200.

[23] X. Zhao, J. Wang, J. Wang, M. Yang, C. Yan, G. Zou, S. T. John, C. Fernandez, Q. Peng, *Cell Rep. Phys. Sci.* **2022**, *3*, 3.

[24] M. Wang, W. Wang, T. Qian, S. Liu, Y. Li, Z. Hou, J. B. Goodenough, M. Ajayan, C. Yan, *Adv. Mater.* **2019**, *31*, 1803339.

Supplementary Information

N-Decorated Main-Group $MgAl_2O_4$ Spinel: Exceptional Oxygen Reduction Activity for Zn-Air Batteries

Xue Zhao[1], *Fengqi Wu*[1], *Haidong Hu*[1], *Jinyu Li*[1], *Yong Sun*[1], *Jing Wang*[1], *Guodong Zou*[*,1], *Xiaobo Chen*[2], *Yong Wang*[3], *Carlos Fernandez*[4], *Qiuming Peng*[*,1]

X. Zhao, F.Q. Wu, H.D. Hu, J.Y. Li, Y. Sun, J. Wang, G.D. Zou, Q.M. Peng

State Key Laboratory of Metastable Materials Science and Technology, Yanshan University, Qinhuangdao, 066004, P.R. China

Corresponding Authors: zouguodong@ysu.edu.cn; pengqiuming@ysu.edu.cn

X.B. Chen

School of Engineering, RMIT University, Carlton 3053, VIC, Australia

Y. Wang

College of Chinese Medicine, Beijing University of Chinese Medicine, Beijing, 100029, China

C. Fernandez

School of Pharmacy and life sciences, Robert Gordon University, Aberdeen,
AB107GJ, United Kingdom

Keywords: spinel; main-group catalyst; ORR; ZABs; recycle

1. Methods

1.1. Catalyst synthesis

The mixed x mg Al and (1-x) mg of Mg powder were treated by ball-milling, the value of x varied from 0.1, 0.2, 0.3, to 0.4. This powder mixture was ball-milled at 400 rpm with 10 consecutive cycles of 30 min segments and 20 min cool-down periods, which was then pyrolyzed at 900 °C under CO/NH_3 (1:1) atmosphere for 5 h with a heating rate of 10 °C min^{-1} in the subsequent process. Finally, $MgAl_2O_4$-N is obtained after acid leaching treatment in a 1M HCl solution for 12 h to remove MgO. In contrast, $MgAl_2O_4$ was synthesized with the same procedure as $MgAl_2O_4$-N yet only CO atmosphere was used instead of CO/NH_3 atmosphere. NC substrate was synthesized in the same way as $MgAl_2O_4$-N, whereas it employed Mg powder instead of a mixture of x mg Al and (1-x) mg of Mg powder. Waste Mg alloys, such as AZ31(Mg-3Al-1Zn), AZ80(Mg-8Al-0.3Zn) and AZ91(Mg-9Al-1Zn) alloys were recycled and processed in the same way as the Mg and Al powders, by direct ball-milling and pyrolysis.

1.2. Materials characterization

The crystal structure was determined using a Rigaku SmartLab X-ray diffractometer with Cu-Kα radiation (λ = 1.5406 Å). The X-ray diffraction (XRD) patterns were refined using the Rietveld refinement program RIETAN-2000. The inductively coupled plasma-mass spectrometry (ICP-MS) was measured by Agilent 7700/7800. The Brunauer-Emitter-Teller (BET) specific surface areas of the materials were obtained using an ASAP Tristar II 3020. The scanning electron microscope (SEM) images were acquired by FEI Helios G4CX with an accelerating voltage of 5 kV. Transmission electron microscopy (TEM), high resolution transmission electron microscopy (HRTEM), and energy-dispersive spectra (EDS) elemental mapping images were collected on a Titan ETEM G2 (scanning/transmission electron microscope) operated at 300 kV. X-ray photoelectron spectroscopy (XPS) data were collected using a Perkin Elmer PHI 1600 ESCA system.

1.3. Electrochemical measurements

The electrochemical analysis of catalysts were carried out using an electrochemical workstation (CHI 760E) equipped with a rotating ring disk electrode (RRDE) system (RRDE-3A, ALS). The glassy carbon (GC) with a diameter of 4 mm served as the support for the working electrode. The graphite rod was employed as the counter electrode and the reference electrode was Hg/HgO electrode (filled with 1 M NaOH solution). The 0.1 M KOH solution electrolyte was prepared using a potassium hydroxide pellet. The neutral electrolyte with a pH = 7 and the weakly acidic electrolyte with a pH = 5 were prepared using different ratios of potassium dihydrogen phosphate and potassium hydrogen phosphate solutions. All the recorded potentials were converted to the reversible hydrogen electrode (RHE)[1].

To prepare catalyst ink, a mixed solution containing 800 μL of deionized water, 200 μL of isopropanol, 30 μL of Nafion solution (5 wt%), and 4 mg of catalyst were thoroughly dispersed by ultrasonication for 40 minutes. The ink was drop-casted onto the disk electrode with a controlled loading of 0.339 mg cm^{-2} and left to dry at room temperature, forming a thin film electrode. Cyclic voltammetry (CV) curves were recorded at a scan rate of 50 mV s^{-1} under Ar and O_2 environments. The accelerated durability (ADT) was obtained at a scan rate of 5 mV s^{-1} in the potential range of 1.2 to 0.2 V (1600 rpm). For the RRDE tests, the hydrogen peroxide yield [H_2O_2 (%)] and the electron transfer number -N were calculated from the linear sweep voltammetry (LSV) at 1600 rpm using the following equation:

$$H_2O_2(\%) = 200 \times \frac{\frac{I_r}{N}}{I_d + \frac{I_r}{N}} \tag{1}$$

$$n = 4 \times \frac{I_d}{I_d + \frac{I_r}{N}} \tag{2}$$

where I_{d} was the disk current, I_{r} was the ring current and N was the current collection efficiency of the platinum ring with a value of 0.4.

1.4. Zinc-air batteries Tests

The aqueous rechargeable zinc-air batteries (ZABs) were assembled and tested using a two-electrode electrochemical device. Catalyst (4 mg), acetylene black (1 mg), XC-72 (4 mg) and Nafion diluent (8 mL) are dissolved in 300 ul isopropyl alcohol by ultrasonication to form a uniform ink drop onto cleaned carbon paper and nickel foam composite electrode to make the air cathode with a loading density of 1 mg cm^{-2}. After preparing the air cathodes, they were placed in a drying oven at 60 °C and set aside. The electrolyte consisted of a mixed solution containing 6.0 M KOH and 0.2 M zinc acetate. Polished zinc foil (0.5 mm) was used as the anode, while the cathode was the carbon paper and nickel foam composite electrode equipped with a gas diffusion layer. The mold for ZABs was purchased from Changsha Spring Company. The polarization curves were generated using a CHI760E electrochemical workstation, and the galvanostatic charge-discharge tests were conducted on a battery measurement system (Land CT2001A). All tests were carried out after 10 h of static treatment. The galvanostatic charge-discharge curves at room temperature with various current densities and the galvanostatic charge-discharge curves of 10 mA cm^{-2} at different temperatures were test after 50 h charge-discharge process with the aim of initially activating the battery and transitioning it into the stabilization phase.

1.5. In-Situ XRD Characterization in ZABs

In-situ XRD measurements were performed on Rigaku SmartLab. The ZABs was assembled using a tailor-made mould with a window that allows X-rays to pass through. The constant galvanostatic charge-discharge curves of the ZABs were measured by the CHI760E electrochemical workstation with a current density of 10 mA cm^{-2}. The XRD patterns were acquired at 10 minute intervals for the same position.

1.6. Computational Methods

All calculations were performed using the projector augmented wave method as implemented in the Vienna ab initio simulation package (VASP)[2]. The exchange-correlation potentials were treated within the generalized gradient approximation according to the Perdew, Burke, and Ernaerhof form[3]. The plane-wave expansion with an energy cutoff of 500 eV was employed. All structural relaxations were performed until the Hellmann-Feynman forces were less than 10^{-5} eV/Å. Brillouin zone with a Gaussian broadening of 0.05 eV were performed. The centered Monkhorst-Pack k-point meshes for sampling the Brillouin zone was 5×5×1. The van der Waals (vdW) interaction was incorporated through the semi-empirical DFT-D2 field method[4]. The Gibbs free energy was calculated as following:

$$\Delta G = \Delta E + \Delta ZPE - T\Delta S \tag{3}$$

where ΔE was the DFT calculated adsorption energy difference from the initial to final states. ΔZPE was the change of zero point energy. T was fixed at 289.15 K in our study and ΔS was the entropy change. The nature of the stationary point and zero point energy (ZPE) corrections was characterized by calculating harmonic vibration frequency. Gibbs free energy change (ΔG_i, i = 1-4) for each elementary step can be summarized as following,

$$\Delta G_1 = 4.92 - \Delta G_{*OOH} \quad (4)$$

$$\Delta G_2 = \Delta G_{*OOH} - \Delta G_{*O} \quad (5)$$

$$\Delta G_3 = \Delta G_{*O} - \Delta G_{*OH} \quad (6)$$

$$\Delta G_4 = \Delta G_{*OH} \quad (7)$$

The theoretical overpotential η^{ORR} for a given electrocatalyst can be evaluated:

$$\eta^{ORR} = 1.23\ V - \min\{\Delta G_1, \Delta G_2, \Delta G_3, \Delta G_4\}/e \quad (8)$$

2. Results and Discussion

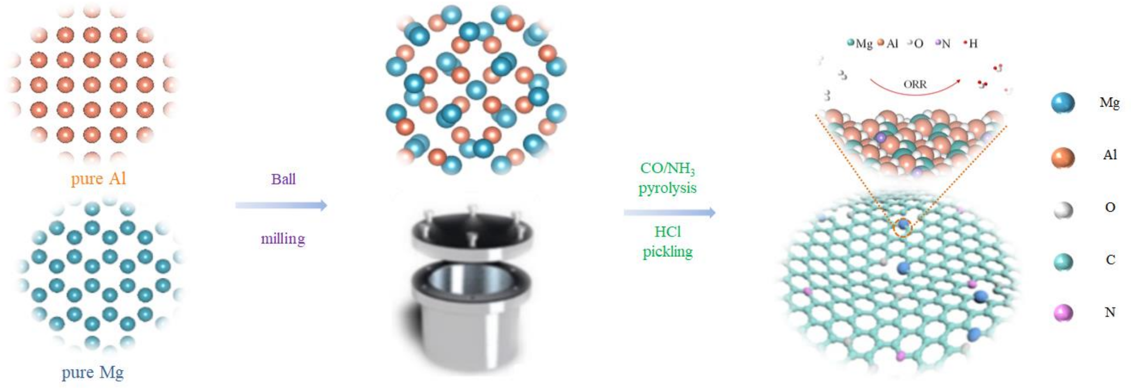

Figure S1. Schematic illustration showing the preparation process of the $MgAl_2O_4$-N.

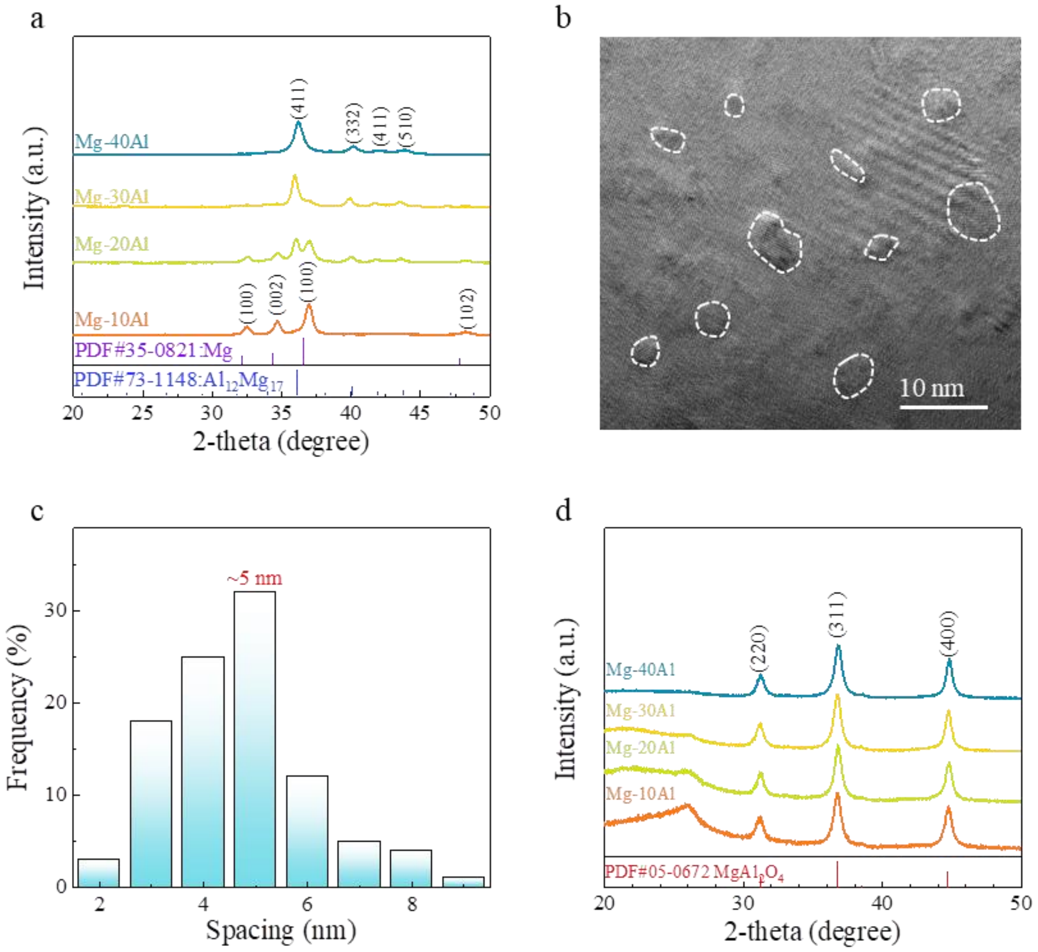

Figure S2. (a) X-ray diffraction (XRD) patterns of the ball milled Mg-10Al, Mg-20Al, Mg-30Al, and Mg-40Al before pyrolysis. (b) High resolution transmission electron microscopy (HRTEM) image of the Mg-20Al, the particles are $Al_{12}Mg_{17}$ solid solution. (c) Size distribution of $Al_{12}Mg_{17}$ particles. (d) XRD patterns of the ball milled Mg-10Al, Mg-20Al, Mg-30Al, and Mg-40Al after pyrolysis at 900 ℃.

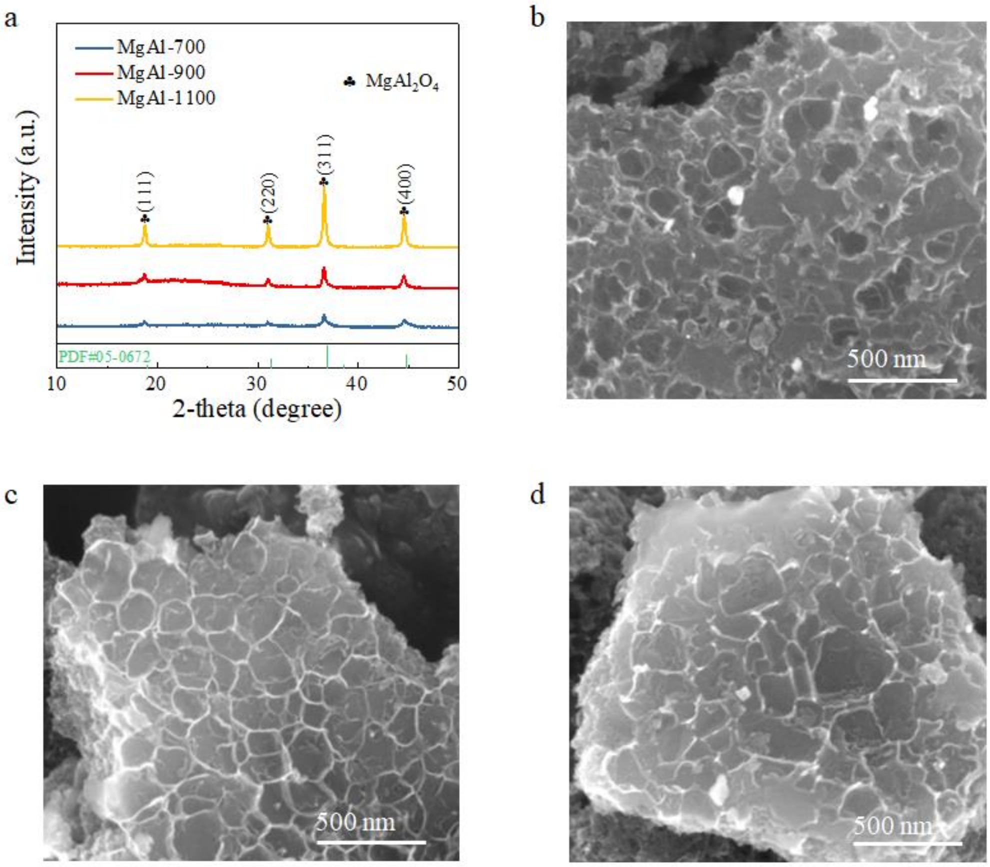

Figure S3. (a) XRD patterns of the Mg-20Al pyrolysis at 700 ℃, 900 ℃, and 1100 ℃, respectively. (b-d) Scanning electron microscope (SEM) image of the Mg-20Al pyrolysis at 700 ℃, 900 ℃, and 1100 ℃, respectively.

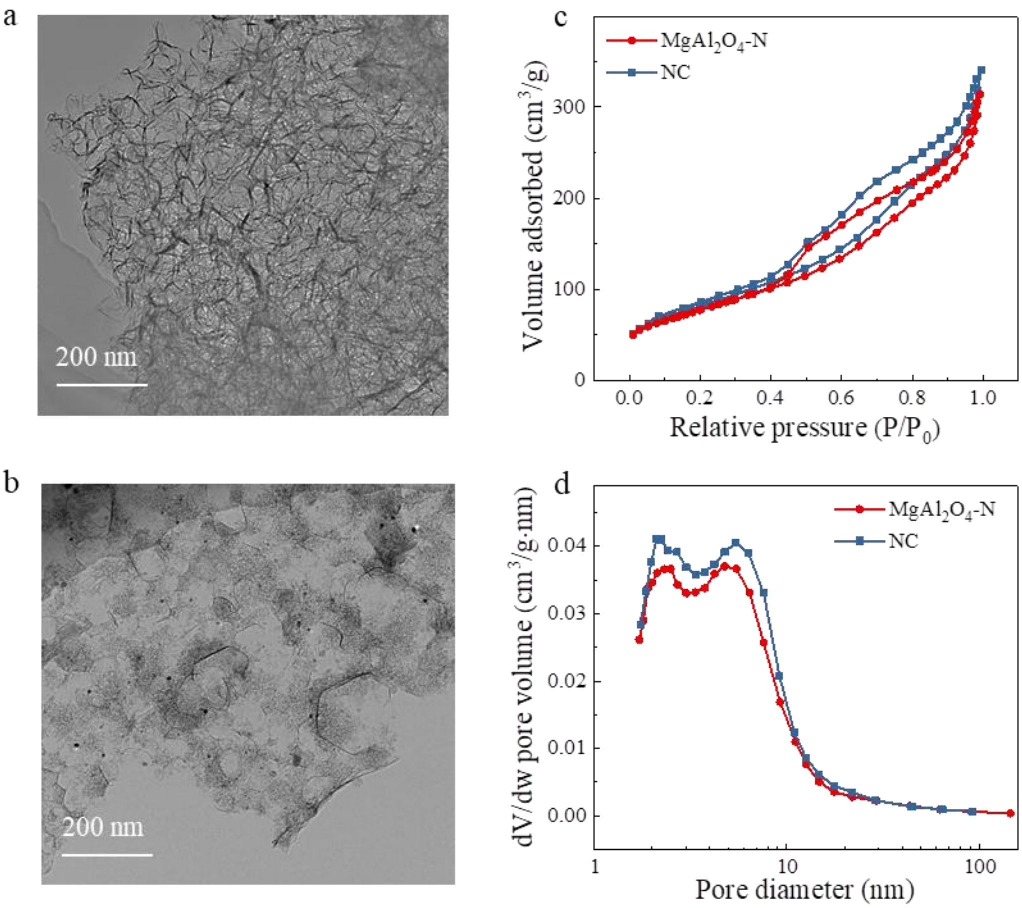

Figure S4. SEM image of the NC (a) and MgAl$_2$O$_4$-N (b). N_2 adsorption/desorption plots (c) and pore distribution (d) of the NC and MgAl$_2$O$_4$-N.

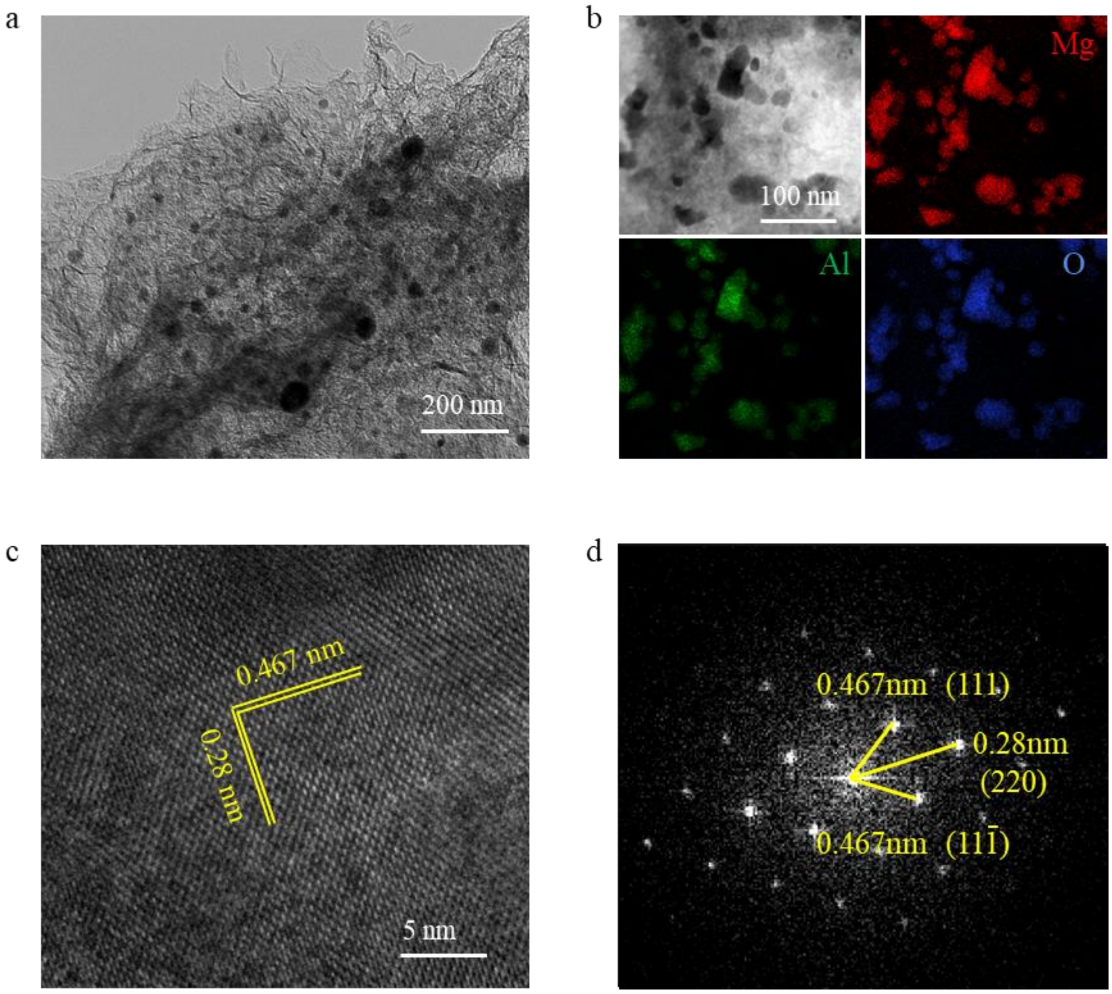

Figure S5. (a) Transmission electron microscopy (TEM) image of the $MgAl_2O_4$ sample. (b) Energy-dispersive spectra (EDS) elemental mapping. (c) HRTEM image sample and corresponding fast fourier transform (FFT) pattern (d).

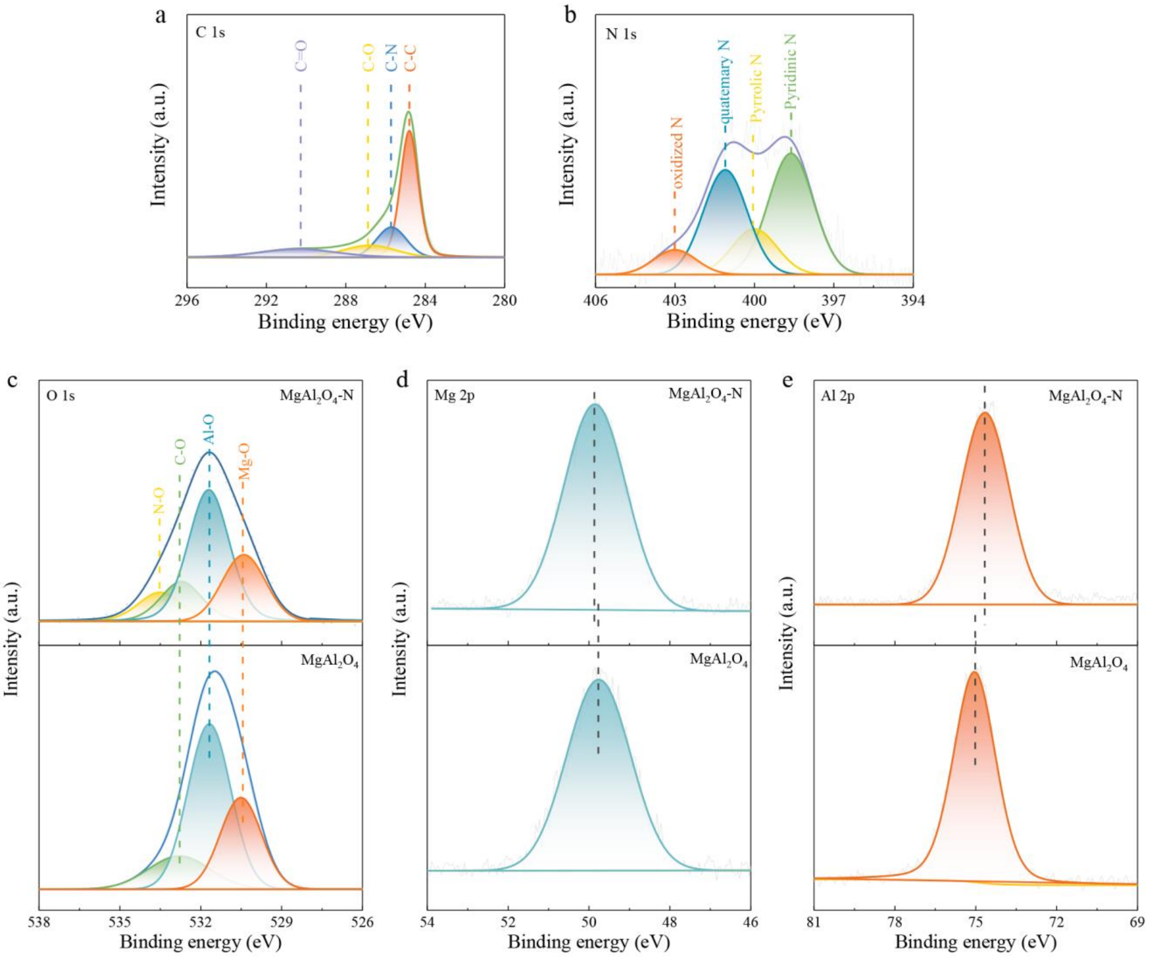

Figure S6. High-resolution XPS spectra of C1s (a) and N1s (b) of $MgAl_2O_4$-N, respectively. High-resolution O1s (c), Mg 2p (d) and Al 2p (e) of $MgAl_2O_4$-N and $MgAl_2O_4$, respectively.

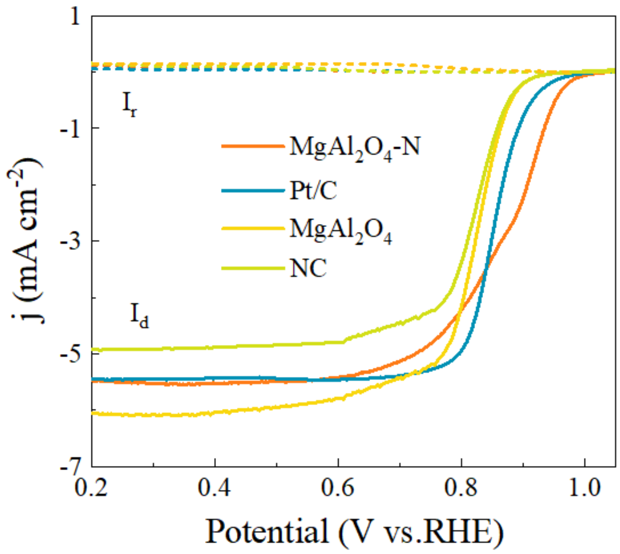

Figure S7. The recorded ring and disk currents of catalysts measured by RRDE measurement.

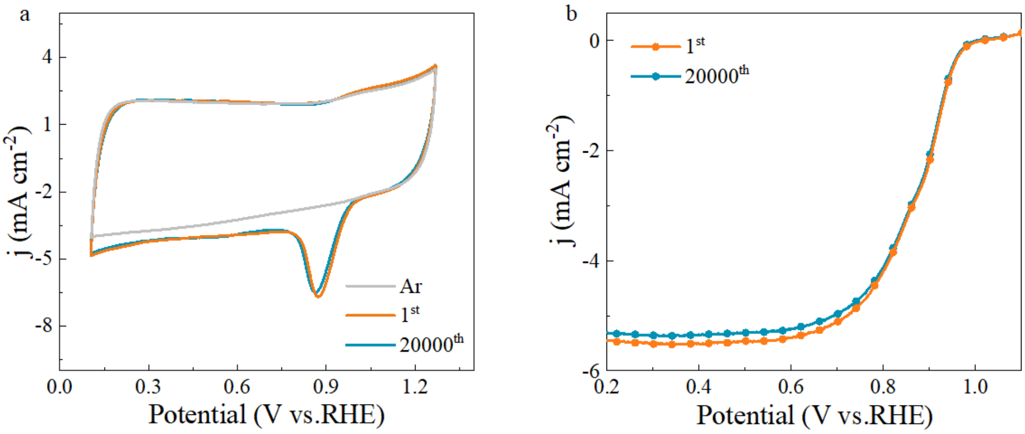

Figure S8. (a) CV and (b) LSV curves of $MgAl_2O_4$-N at Ar and before and after ADT testing at O_2 in 1.0 M KOH solution.

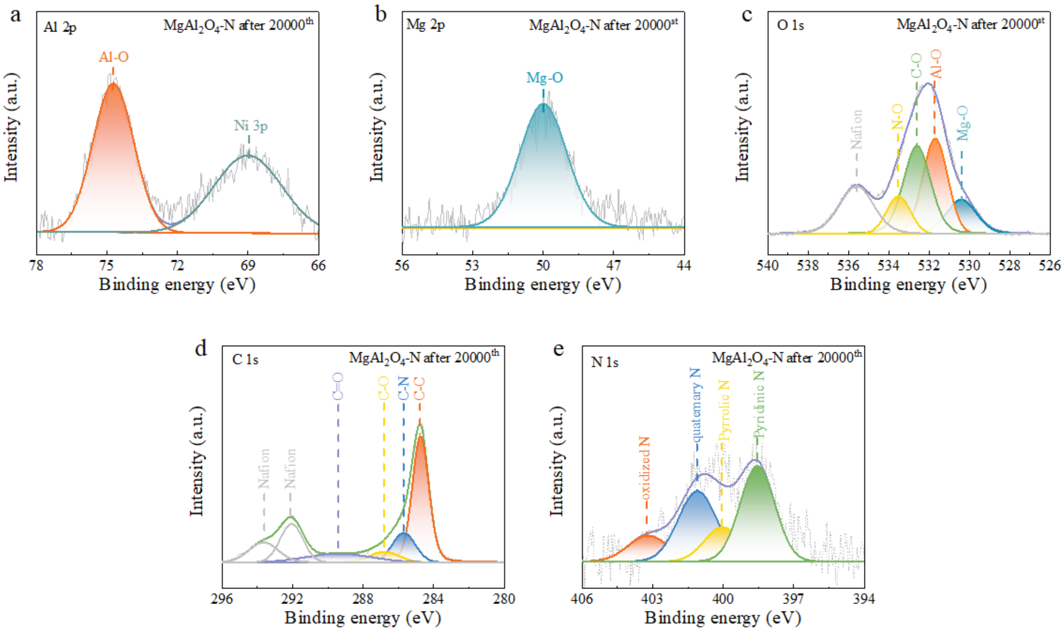

Figure S9. XPS spectroscopy of of $MgAl_2O_4$-N after 20000 cycles in a 0.1 M KOH solution. High-resolution XPS spectra of Al 2p (a), Mg 2p (b), O 1s (c), C 1s (d), and N 1s (e).

The CV cycling test was performed by mixing the catalyst and binder Nafion and then coating it on nickel foam. In the XPS spectra of Al 2s, additional peaks appeared that can be attributed to the Ni 3p peaks of the nickel foam[5]. The proximity of these two peaks allows the XPS signal of Ni 3p to appear in the Al 2s spectrum. And in the XPS spectra of O 1s, the added peaks can be attributed to the O 1s peaks of the binder

Nafion[6].

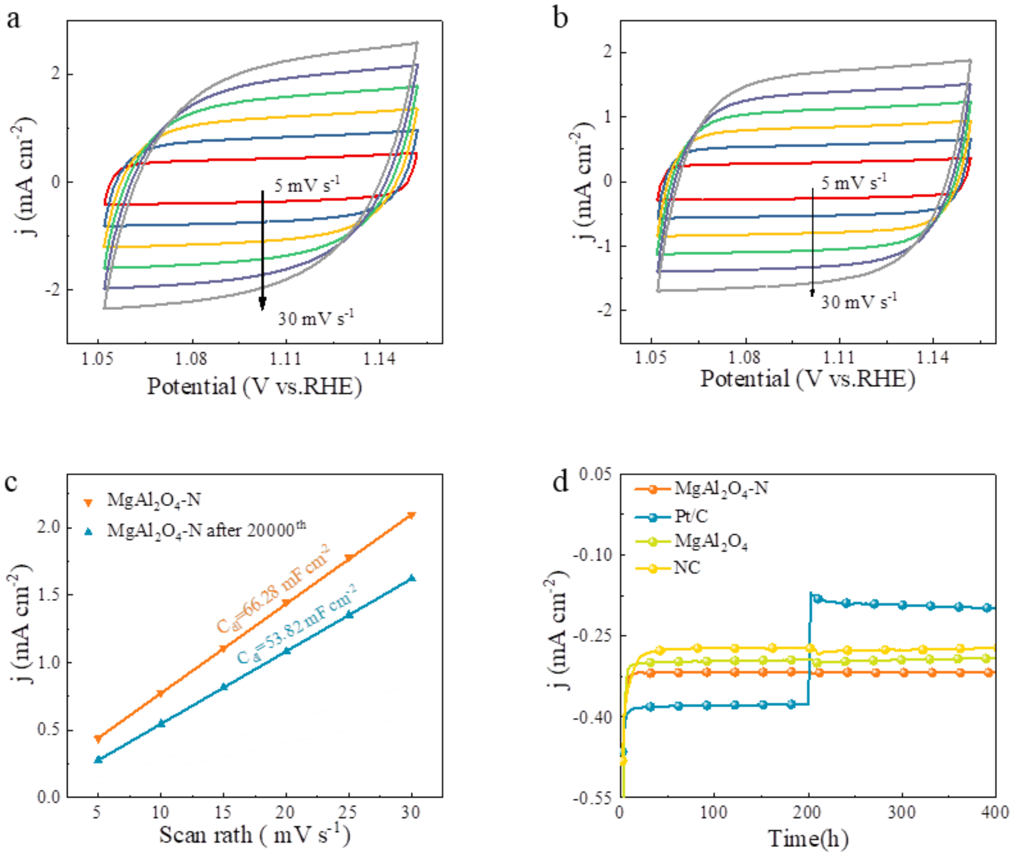

Figure S10. CV at various scan rates (5-30 mV·s^{-1}) in 1.0 M KOH solution before (a) and after (b) ADT testing. (c) The C_{dl} for catalysts. (d) The chronoamperometry (CA) measurements were carried out by adding CH_3OH (0.01 M) into the 1.0 M KOH solution.

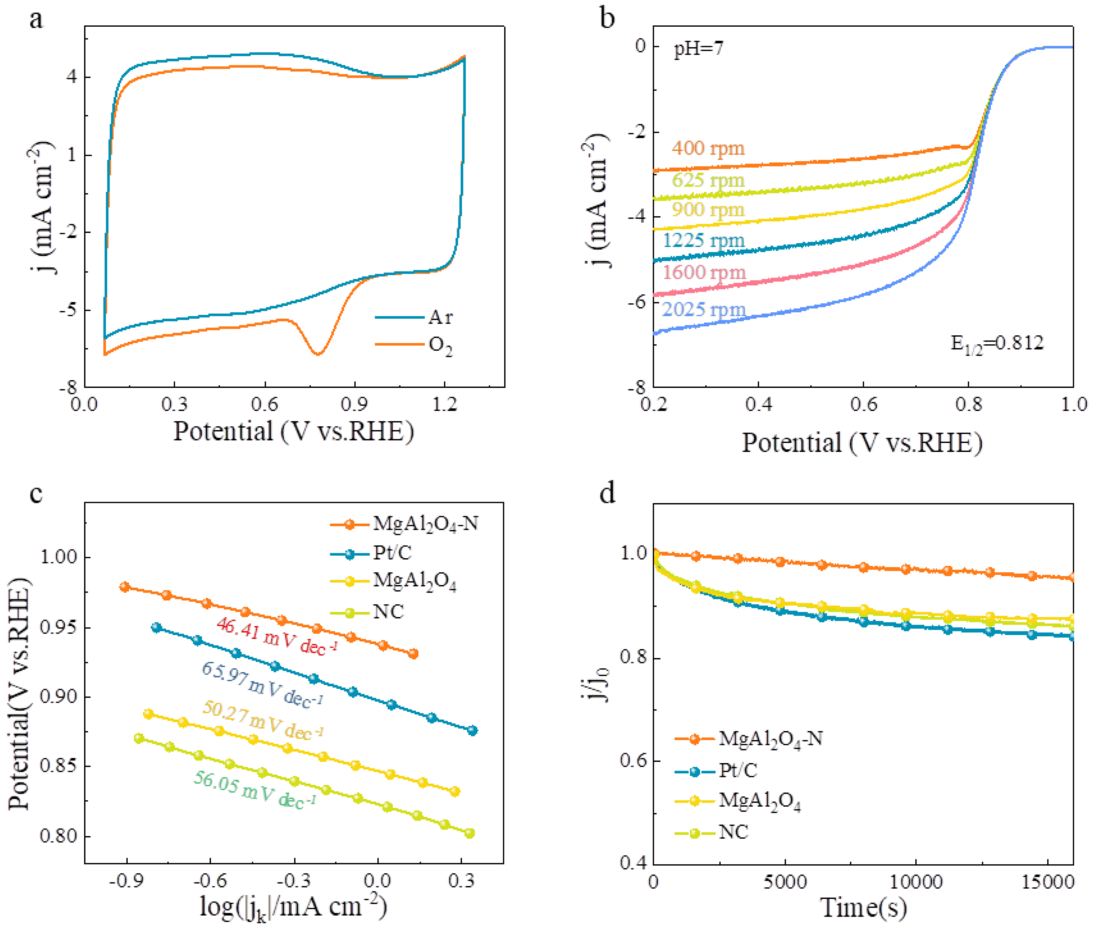

Figure S11. Electrochemical tests of $MgAl_2O_4$-N in the pH = 7 neutral electrolyte. (a) CV curves, (b) LSV curves, (c) Tafel plots, and (d) CA test of the catalysts at 0.6 V.

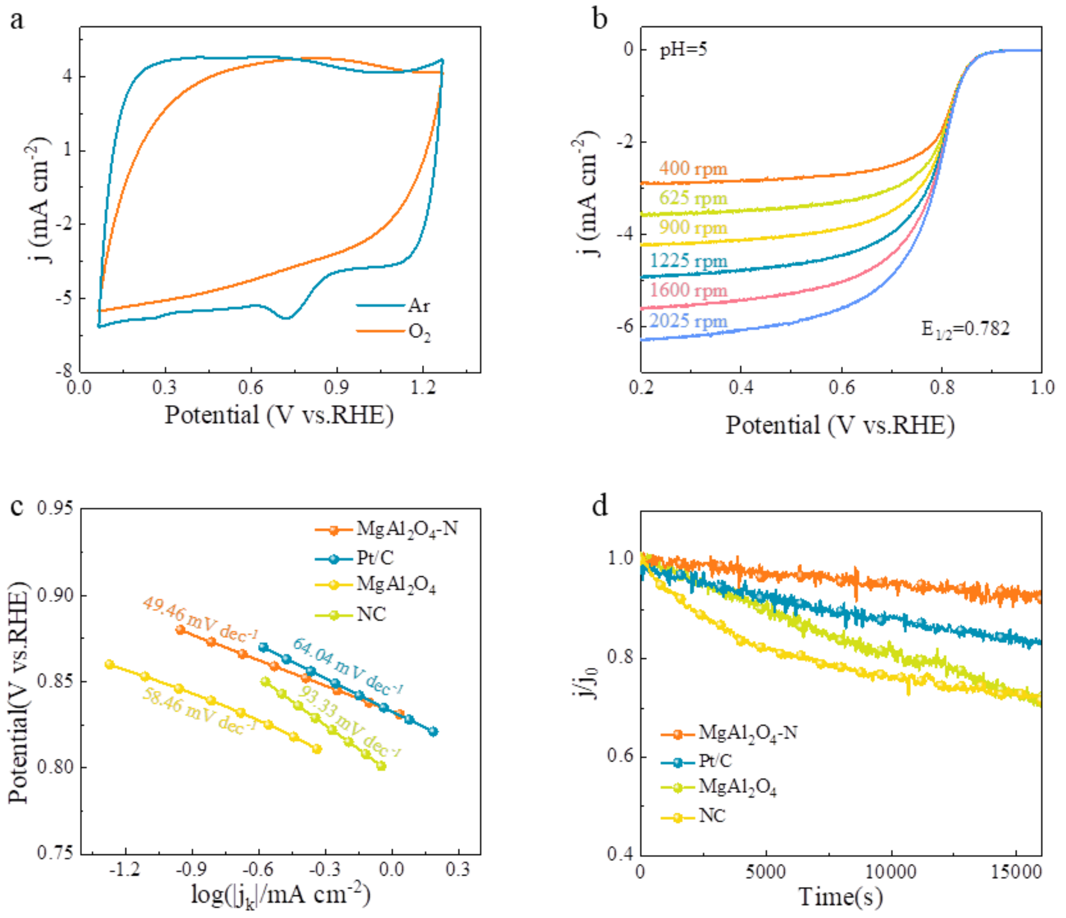

Figure S12. Electrochemical tests of $MgAl_2O_4$-N in the weakly acidic electrolyte. (a) CV curves within a potential range from 0 to 1.2 V (scan rate: 50 mV s^{-1}), (b) LSV curves, (c) Tafel plots, and (d) CA test of the catalysts at 0.6 V.

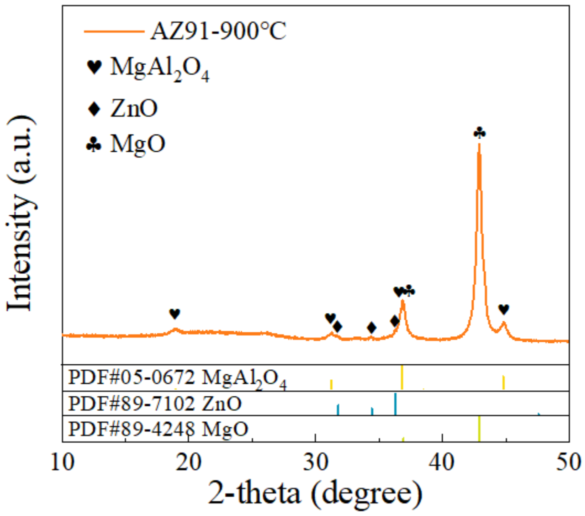

Figure S13. XRD patterns of the AZ91 pyrolysis at 900 ℃ before pickling.

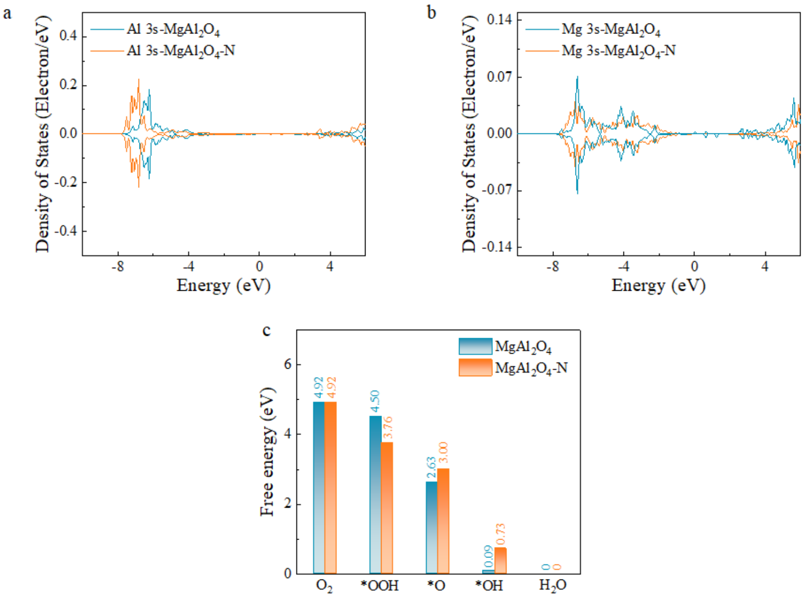

Figure S14. PDOS profiles for $MgAl_2O_4$ and $MgAl_2O_4$-N. (a) Al 3s. (b) Mg 3s. (c) The numerical energy profile values of catalysts.

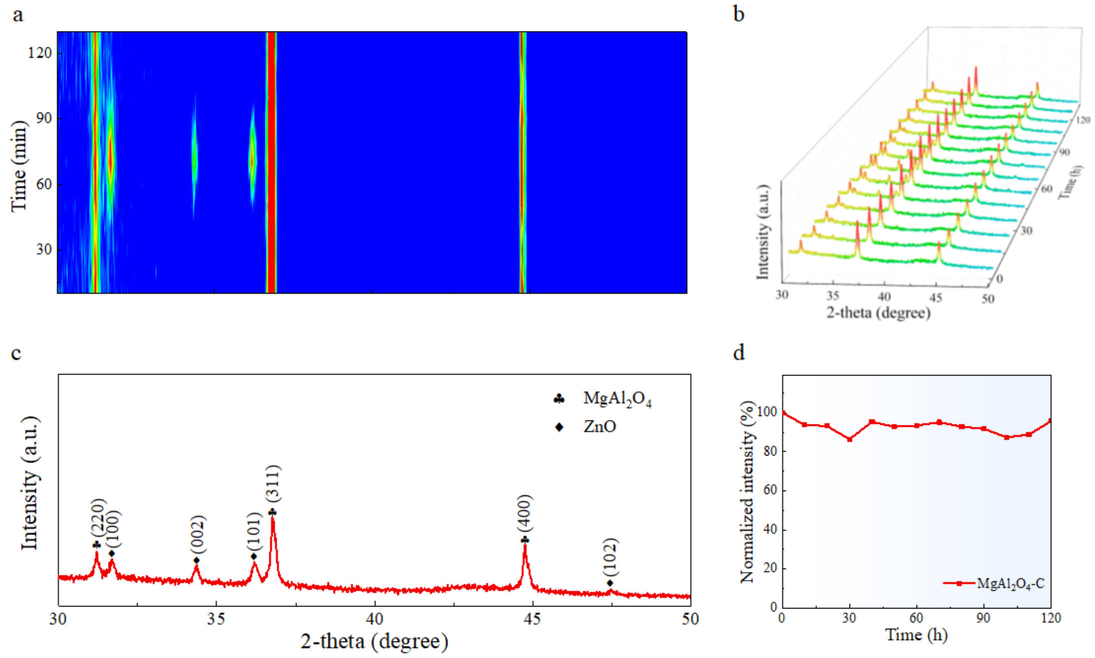

Figure S15. (a) *In-situ* XRD intensity map of ZABs with $MgAl_2O_4$. (b) Corresponding *in-situ* XRD patterns of ZABs with $MgAl_2O_4$. (c) XRD patterns at 60min during discharge. (d) Intensity changes of $MgAl_2O_4$ peak at 36.70 ° during ZABs operation.

Supplementary Table 1 Metal concentration in the different samples determined by ICP-MS.

Samples	Metal	concentration (wt.%)
$MgAl_2O_4$-N	Mg	11.65
	Al	21.83
$MgAl_2O_4$	Mg	12.53
	Al	24.98

Supplementary Table 2 Chemical composition of the $MgAl_2O_4$-N recorded by XPS.

Elements	Assignment	Position (eV)	Content (at.%)
Mg	Mg-O	49.87	9.30
Al	Al-O	74.62	18.59
O	Mg-O	530.47	10.92
	Al-O	531.68	21.93
	C-O	532.76	6.03
	N-O	533.50	5.21
N	Pyridinic N	398.61	1.24
	Pyrrolic N	399.94	0.53
	quatemary N	401.11	1.05
	oxidized N	403.02	0.40
C	C-C	284.77	13.17
	C-N	285.9	3.78
	C-O	286.86	3.90
	C=O	290.52	3.95

Supplementary Table 3 Chemical composition of the $MgAl_2O_4$ recorded by XPS.

Elements	Assignment	Position (eV)	Content (at.%)

Mg	Mg-O	49.78	11.02
Al	Al-O	75.01	22.30
O	Mg-O	530.47	12.31
	Al-O	531.68	25.89
	C-O	532.82	6.59
C	-	-	20.05

Supplementary Table 4 Chemical composition of the $MgAl_2O_4$-N after 20000 cycles recorded by XPS.

Elements	Assignment	Position (eV)	Content (at.%)
Mg	Mg-O	49.86	5.41
Al	Al-O	74.71	10.81
	Nafion	69.05	13.57
O	Mg-O	530.40	6.18
	Al-O	531.72	12.89
	C-O	532.65	14.30
	N-O	533.52	4.89
	Nafion	535.61	9.75
N	Pyridinic N	398.61	1.07
	Pyrrolic N	399.94	0.73

	quaternary N	401.11	0.98
	oxidized N	403.02	0.68
C	C-C	284.77	6.31
	C-N	285.9	1.81
	C-O	286.86	2.34
	C=O	290.52	2.85
	Nafion	292.08	2.88
	Nafion	293.64	2.55

Supplementary Table 5 Comparison of ORR performance in 0.1 M KOH and performance of ZABs of $MgAl_2O_4$-N with reported electrocatalysts.

Catalyst	ORR $E_{1/2}$(V)	Cyclability (h)	Power density (mW cm^{-2})	Ref.
$MgAl_2O_4$-N	0.881	2000	158.5	This work
Co_4N@CoON/PCGN	0.855	1350	153	[7]
FeNiAC-NC	0.936	1000	101.4	[8]
Fe/SNCFs-NH_3	0.89	1000	255.84	[9]
Co_2FeO_4/NCNTs	0.8	100	90.68	[10]
NiFe-LDH/Co	0.79	80	25	[11]
Co-Co_3O_4@NAC	0.795	35	164	[12]
FeCo@MNC	0.86	24	115	[13]

$CoMn_2O_4$/NCNTs@Ni	0.80	238	95.77	[14]
N-Co/CNF-300-10	0.853	25	229	[15]
Fe_1Co_1-CNF	0.87	200	201.7	[16]
Co-NiO NFs	0.79	110	93	[17]
0.1-Co–NHCs	0.81	50	239.8	[18]
PB@Met-700	0.853	90	148	[19]
3DOM-$Mg_xCo_{3-x}O_4$	0.839	236	253	[20]

Supplementary References

[1] A. Kumar, V.Q. Bui, J. Lee, L. Wang, A.R. Jadhav, X. Liu, X. Shao, Y. Liu, J. Yu, Y. Hwang, H.T.D. Bui, S. Ajmal, M.G. Kim, S.-G. Kim, G.-S. Park, Y. Kawazoe & H. Lee, *Nat. Commun.* **2021**, 12, 6766.

[2] a) G. Kresse, J. Hafner, *Phys. Rev. B* **1993**, 47, 558; b) P. E. Blöchl, *Phys. Rev. B* **1994**, 50, 17953.

[3] J. P. Perdew, K. Burke, M. Ernzerhof, *Phys. Rev. Lett.* **1996**, 77, 3865.

[4] E. Jung, H. Shin, B.-H. Lee, V. Efremov, S. Lee, H. S. Lee, J. Kim, W. Hooch Antink, S. Park, K.-S. Lee, *Nat. Mater.* **2020**, 19, 436.

[5] X. Xie, A. Sandhya, L. Piliai, M. Vorokhta, I. Matolínová, I. Khalakhan, *Appl Catal B-Environ.* **2023**, 325, 122328.

[6] A. Friedman, W. Shi, Y. Losovyj, A. Siedle, L. Baker, *J. Electrochem. Soc.* **2018**, 165, H733.

[7] M. Park, J. Hwang, Y. Deng, D. Lee, J. Fu, Y. Hu, M. Jang, S. Choi, R. Feng, G. Jiang, L. Qian, Q. Ma, L. Yang, Y. Jun, M. Seo, Z. Bai, Z. Chen, *Adv. Mater.* **2023**, 2311105.

[8] Y. Wang, N. Katyal, Y. Tang, H. Li, K. Shin, W. Liu, R. He, M. Xu, G. Henkelman, S. Bao, *Small* **2023**, 2306504.

[9] L. Yang, X. Zhang, L. Yu, J. Hou, Z. Zhou, R. Lv, *Adv. Mater.* **2022**, 34 2105410.

[10] X.-T. Wang, T. Ouyang, L. Wang, J.-H. Zhong, T. Ma, Z.-Q. Liu, *Angew. Chem. Int. Ed.* **2019**, 58 13291.

[11] Q. Wang, L. Shang, R. Shi, X. Zhang, Y. Zhao, G.I.N. Waterhouse, L.-Z. Wu, C.-H. Tung, T. Zhang, *Adv. Energy Mater.* **2017**, 7, 1700467.

[12] X. Zhong, W. Yi, Y. Qu, L. Zhang, H. Bai, Y. Zhu, J. Wan, S. Chen, M. Yang, L. Huang, M. Gu, H. Pan, B. Xu, *Appl Catal B-Environ.* **2020**, 260, 118188.

[13] C. Li, M. Wu, R. Liu, *Appl Catal B-Environ.* **2019**, 244, 150.

[14] H. Su, X.-T. Wang, J.-X. Hu, T. Ouyang, K. Xiao, Z.-Q. Liu, *J. Mater. Chem. A* **2019**, 7, 22307.

[15] P. Rao, P. Cui, Z. Wei, M. Wang, J. Ma, Y. Wang, X. Zhao, *ACS Appl. Mater. Interfaces* **2019**, 11, 29708.

[16] Y. Wang, Z. Li, P. Zhang, Y. Pan, Y. Zhang, Q. Cai, S.R.P. Silva, J. Liu, G. Zhang, X. Sun, Z. Yan, *Nano Energy* **2021**, 87, 106147.

[17] J. Qian, X. Guo, T. Wang, P. Liu, H. Zhang, D. Gao, *Appl Catal B-Environ.* **2019**, 250, 71.

[18] S. Chen, J. Cheng, L. Ma, S. Zhou, X. Xu, C. Zhi, W. Zhang, L. Zhi, J.A. Zapien,

Nanoscale **2018**, 10, 10412.

[19] Y. Lian, K. Shi, H. Yang, H. Sun, P. Qi, J. Ye, W. Wu, Z. Deng, Y. Peng, *Small* **2020**, 16, 1907368.

[20] Y. Zhang, Z. Zhang, G. Jiang, A. Mamaghani, S. Sy, R. Gao, Y. Jiang, Y. Deng, Z. Bai, L. Yang, A. Yu, Z. Chen, *Nano Energy* **2022**, 100, 107425.